IEEE Access
Multidisciplinary | Rapid Review | Open Access Journal

Date of publication xxxx 00, 0000, date of current version xxxx 00, 0000.

Digital Object Identifier 10.1109/ACCESS.2022.Doi Number

Discontinuous Conduction Mode Analysis of Two-Phase Interleaved Buck Converter with Inversely Coupled Inductor

HYE-CHEON KIM[1], (Student Member, IEEE), MRIGANKA BISWAS[2], (Member, IEEE), AND JUNG-WOOK PARK[1], (Senior Member, IEEE)

[1]School of Electrical and Electronic Engineering, Yonsei University, Seoul 03722, South Korea
[2]School of Engineering, The University of Edinburgh, Edinburgh EH9 3FG, U.K.

Hye-Cheon Kim and Mriganka Biswas are the co-first authors. Corresponding author: Jung-Wook Park (e-mail: jungpark@yonsei.ac.kr).

This work was supported by the National Research Foundation (NRF) (Grant number: 2020R1A3B2079407), the Ministry of Science and ICT (MSIT), Korea.

ABSTRACT This study comprehensively analyzes the discontinuous conduction mode (DCM) of a two-phase interleaved buck converter (IBC) with an inversely coupled inductor (ICL). With ICL, nine circuit configurations are possible when the IBC operates in the DCM. Depending on the duty ratio and load condition, DCM can also be classified into seven types. Each type of DCM has a corresponding combination of circuit configurations. Consequently, the application of the combinations for distinguishing DCM types is proposed to analyze the DCM operation of two-phase IBCs with ICL. Different DCM types have different DCM characteristics, such as state space averaged models and time interval calculations, which are needed to be analyzed for small-signal modeling. Therefore, the state space averaged models and time intervals equations are derived for each DCM type, and boundary conditions between adjacent DCM types are analyzed. Experimental tests on the hardware prototype of the IBC are conducted to verify the practical effectiveness of the proposed analysis.

INDEX TERMS Buck converter, coupled inductor, discontinuous conduction mode, interleaved, time interval, voltage gain, state space averaged model.

I. INTRODUCTION

Buck converters are one of the most common power converters for voltage regulation. Among various buck topologies, the interleaving topology is able to improve the efficiency and power density of converter [1]–[5]. However, it has the disadvantage of increasing the number of inductors. Therefore, the coupled inductor (CL), which can reduce the number of inductor cores, has been used to improve the power density while decreasing inductor current ripples [6]–[9]. In particular, the use of inversely coupled inductor (ICL) among CLs can effectively improve the efficiency [10]–[11].

Although most converters with ICLs have been generally designed in the continuous conduction mode (CCM) [12]–[16], they might be subject to operate in the discontinuous conduction mode (DCM) under a wide range of operating condition for practical applications, such as renewable energy and electric vehicle, etc [9], [17]–[18]. To deal with this problem, its operation in the DCM must be carefully analyzed. In particular, the interleaved buck converter (IBC) with ICL has several types of DCM depending on load condition, switching frequency, and coupling factor. Then, the analysis of IBC in the DCM becomes more challenging [18]–[22]. In addition, their state space averaged model, time interval calculations and voltage gains are different [21], [23]. As a result, they are also required to analyze for all types of DCM. Furthermore, they must be estimated in advance before designing the controller of IBC. However, state space averaged models of IBC and IBC with ICL has been studied in only CCM operation [24]–[25]. Therefore, state space averaged model of all DCM types must be also analyzed for comprehensive DCM analysis of IBC with ICL. On the other hand, many studies on multi-phase boost converters [18]–[21] have addressed the challenges caused by CLs, while evaluating the operation of DCM. However, they did not give the systematic analysis of IBC in the DCM but analyzed only interleaved boost converter in the DCM. Also, time interval calculation of IBC in the DCM is

necessary for small-signal modeling. However, there is very few studies to calculate the time intervals for different DCM types of interleaved boost converter [18], [20]. Furthermore, there is no study on the time interval calculation of IBC in the DCM. Moreover, the dual-IBC with the inter-phase transformer was presented in [22]. However, it is only limited to the CLs with strong coupling factor and filter inductors. It is necessary to conduct an analysis considering strong and loose coupling factors to assess control performance. Because the output current does not change even when duty ratio changes in certain DCM region of the IBC, and this region becomes wider as the coupling factor increases. Furthermore, the use of filter inductor can reduce the overall power density.

This study proposes a new method for classifying various DCM types of two-phase IBC using ICL. In particular, it systematically analyzes the two-phase IBC with ICL in all different types of DCM, while deriving associated equations for the state space averaged model and time intervals based on the corresponding circuit configurations of the two-phase IBC with ICL. The remainder of this paper is organized as follows. Section II describes nine circuit configurations when the converter operates in the DCM as well as seven different DCM types of two-phase IBC with ICL. In Section III, mathematical analysis of two-phase IBC with ICL is provided to derive state space averaged model and the time interval calculations, and it is verified through simulation. Then, Section IV analyzes the boundary conditions between adjacent DCM types. Thereafter, the effectiveness of proposed analysis is verified by experimental tests on a hardware prototype in Section V. Finally, the conclusion is given in Section VI.

II. TWO-PHASE IBC WITH ICL IN DCM

The two-phase IBC with ICL is shown in Fig. 1. The input voltage (v_{in}) source is paired with the input filter capacitor, C_{in}. Two parallel power switches (Q_1 and Q_2) with reverse-paralleled diodes are connected to v_{in}, and their respective gate-source voltages (v_{gs1} and v_{gs2}) are operated by the same ON-time duty ratio (d_1) with the phase difference of 180°. Also, Q_1 and Q_2 are connected to diodes D_1 and D_2, respectively, followed by the corresponding inductors, L_1 and L_2. Note that they are magnetically inversely coupled. The currents flowing through each inductor branch are i_{L1} and i_{L2}. The voltages across each inductor branch are denoted by v_{L1} and v_{L2}. Then, the mutual inductance, M can be expressed as the function of coupling factor, k between L_1 and L_2 as

$$M = k\sqrt{L_1 \cdot L_2} \tag{1}$$

The rear end of ICL is connected to the output filter (C_o) in parallel with the load resistance (R_o). The voltage across R_o is represented as v_o. Assume that the self-inductance of two inductors is equal to L (i.e., $L_1 = L_2 = L$), and all components of two-phase IBC with ICL are ideal. Then, the generalized circuit equations of ICL are represented as

$$\begin{cases} v_{L1} = L_1 \dfrac{di_{L1}}{dt} - M\dfrac{di_{L2}}{dt} = L\dfrac{di_{L1}}{dt} - k\cdot L\dfrac{di_{L2}}{dt} \\ v_{L2} = L_2 \dfrac{di_{L2}}{dt} - M\dfrac{di_{L1}}{dt} = L\dfrac{di_{L2}}{dt} - k\cdot L\dfrac{di_{L1}}{dt} \end{cases}. \tag{2}$$

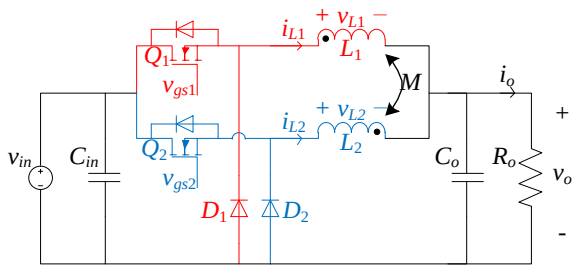

FIGURE 1. Two-phase IBC with ICL.

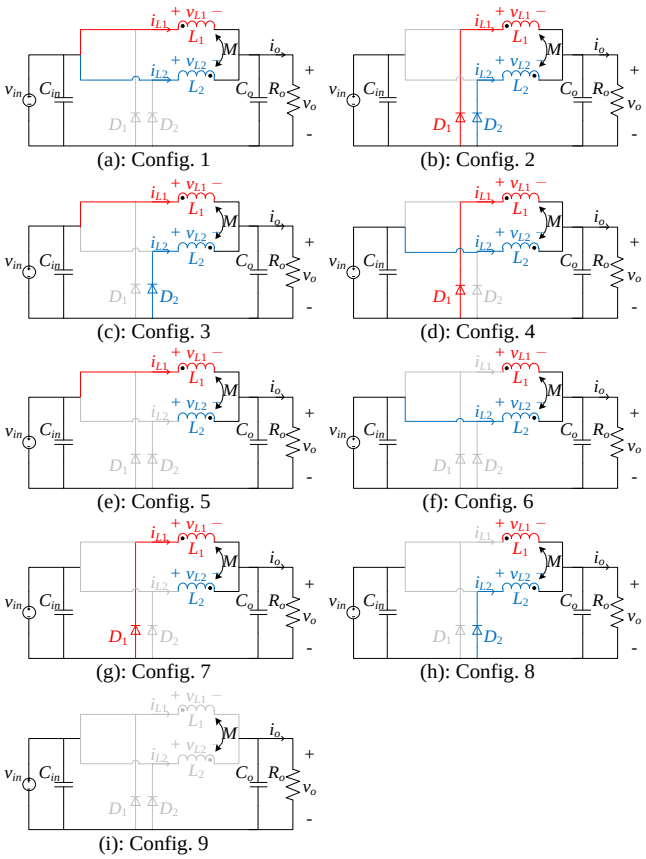

FIGURE 2. All possible circuit configurations of two-phase IBCs with ICL in the DCM: (a) Config. 1, (b) Config. 2, (c) Config. 3, (d) Config. 4, (e) Config. 5, (f) Config. 6, (g) Config. 7, (h) Config. 8, and (i) Config. 9.

A. CIRCUIT CONFIGURATIONS

Due to the ICL effect, the circuit of two-phase IBC with ICL can be configured depending on the states of Q_1 and Q_2, of which each inductor current flows and passes through power switch or diode, as shown in Fig. 2. More details are explained as follows.

• Config. 1: When Q_1 and Q_2 are ON, i_{L1} and i_{L2} flow to the load through Q_1 and Q_2, respectively, as indicated in Fig. 2(a). Simultaneously, D_1 and D_2 are reverse-biased.

• Config. 2: When Q_1 and Q_2 are OFF, and D_1 and D_2 are forward-biased, i_{L1} and i_{L2} flow to the load through D_1 and D_2, respectively, as illustrated in Fig. 2(b)

• Config. 3: When Q_1 is ON, and D_1 is reverse-biased, i_{L1} flows toward the load through Q_1. When Q_1 is OFF, and D_1 is reverse-biased, i_{L1} flows to the input source through the reverse-paralleled diode of Q_1, as shown in Fig. 2(c). At the same time, Q_2 is OFF, and D_2 is forward-biased. Thus, i_{L2} flows to the load through D_2.

• Config. 4: As shown in Fig. 2(d), this operation is opposite to that of Config. 3.

• Config. 5: In this case, D_1 and D_2 are reverse-biased. When Q_1 and Q_2 are ON and OFF, respectively, i_{L1} flows into the load through Q_1. When Q_1 and Q_2 are OFF, i_{L1} flows toward the input source through reverse-paralleled diode of Q_1. The circuit configuration is shown in Fig. 2(e).

• Config. 6: As in Config. 5, D_1 and D_2 are reverse-biased. Also, when both Q_1 and Q_2 are OFF and ON, respectively, i_{L2} flows into the load through Q_2. When both Q_1 and Q_2 are OFF, i_{L2} flows to the input source through reverse-paralleled diode of Q_2. It is shown in Fig. 2(f).

• Config. 7: If both Q_1 and Q_2 are OFF, D_1 is forward-biased, and D_2 is reverse-biased. Then, only i_{L1} flows to the load through D_1, as shown in Fig. 2(g).

• Config. 8: If D_2 and D_1 are forward and reverse-biased, respectively, while keeping both Q_1 and Q_2 OFF, only i_{L2} flows to the load through D_2, as shown in Fig. 2(h).

• Config. 9: When all active components (Q_1, Q_2, D_1, and D_2) are OFF, i_{L1} and i_{L2} do not flow, as illustrated in Fig. 2(i).

Finally, for all circuit configurations shown in Fig. 2, v_{L1} and v_{L2} are summarized in Table I.

TABLE I
INDUCTOR VOLTAGES IN EACH CIRCUIT CONFIGURATION

Circuit Configuration	v_{L1}	v_{L2}
1	$v_{in}-v_o$	$v_{in}-v_o$
2	$-v_o$	$-v_o$
3	$v_{in}-v_o$	$-v_o$
4	$-v_o$	$v_{in}-v_o$
5	$v_{in}-v_o$	$k(v_o-v_{in})$
6	$k(v_o-v_{in})$	$v_{in}-v_o$
7	$-v_o$	$k\cdot v_o$
8	$k\cdot v_o$	$-v_o$
9	0	0

B. DCM TYPES OF TWO-PHASE IBC WITH ICL

When operating the IBC through open-loop control, seven DCM types appear depending on d_1 and load condition. Seven DCM types are shown in Fig. 3 according to d_1 and R_o, whereas v_{in}, L, k, and switching frequency (f_s) are constant. However, when controlling v_o through closed-loop controller while adjusting load condition with same parameters, it can be seen that six DCM types appear, as shown in Fig. 4. Then, the theoretical waveforms of v_{gs1}, v_{gs2}, v_{L1}, v_{L2}, i_{L1}, and i_{L2} for each DCM type are shown in Fig. 5.

It is observed from Fig. 5 that each DCM type has different combination of circuit configurations shown in Fig. 2. One switching period (T_s) is divided into n intervals based on time instants from t_0 to t_n. At each time instant, the circuit configuration is changed from one to another. In particular, they can be expressed by using d_1 as well as first and second inductor current conduction-time ratios, which are d_2 and d_3. In other words, the time instants can be obtained if values of d_1, d_2, and d_3 are known. Also, the value of v_{L1} for each DCM type can be different depending on v_o as given in (2). Likewise, the values of v_{L2} for each DCM type can be different. Therefore, even in the same circuit configuration, i_{L1} and i_{L2} can increase or decrease for each DCM type. Note that the variation in the inductor current slope do not affect the DCM type classification because the proposed analysis method distinguishes DCM types based on the combination of inductor voltages. In addition, the characteristics and time instants for each DCM type are summarized as follows.

• DCM-I: If R_o is beyond the CCM boundary condition and $d_1 < 0.5$, the IBC with ICL may operate from DCM-I to DCM-VI. The waveforms in the DCM-I are shown in Fig. 5(a). The time instants at which the circuit configuration changes are given in Table II. The corresponding circuit configurations at each interval in this type are Configs. 3, 2, 7, 4, 2, and 8.

• DCM-II: It differs from previous DCM type by having two points, where i_{L1} becomes zero at d_2T_s and d_3T_s, as shown in Fig. 5(b). Also, T_s comprises nine time instants, as listed in Table II, by dividing it into eight intervals. Then, the circuit configurations for each interval correspond to Configs. 3, 2, 7, 9, 4, 2, 8, and 9.

• DCM-III: It occurs due to further variation of load and d_1. As shown in Fig. 5(c), there are six time intervals in this DCM type, and their time instants are given in Table II. The corresponding configurations are Configs. 3, 5, 7, 4, 6, and 8.

• DCM-IV: Due to further variations of R_o and d_1, it might occur, as shown in Fig. 5(d) where i_{L1} becomes zero only at d_2T_s. Similarly to the DCM-I and DCM-III, T_s is divided into six intervals by seven time instants given in Table II, where each circuit configuration (Configs. 5, 7, 9, 6, 8, and 9) changes.

• DCM-V: Like DCM-II, this DCM type also consists of eight time intervals with nine time instants listed in Table II

because i_{L1} becomes zero at two points, d_2T_s and d_3T_s, as shown in Fig. 5(e). The equivalent circuit configurations for each interval are Configs. 5, 4, 6, 9, 6, 3, 5, and 9.

• DCM-VI: It is characterized by two points where i_{L1} becomes zero. However, the circuit configuration changes at only one point, at which i_{L1} becomes zero and the inductor voltage changes simultaneously, and it is denoted by d_2T_s, as shown in Fig. 5(f). The entire T_s has five time intervals with six time instants given in Table II, where each circuit configuration (Configs. 5, 4, 6, 3, and 5) changes. In Fig. 4, this DCM type does not appear because a change in d_1 does not induce a change in output current [20].

• DCM-VII: When the load condition is light enough for the converter to operate in the DCM and $d_1 > 0.5$, the IBC with ICL operates in this mode. The associated waveforms are shown in Fig. 5(g). Depending on the v_{L1} and v_{L2} responses, there are six time intervals in T_s, as shown in Fig. 2, and they are given in Table II. The corresponding circuit configurations for six time intervals are Configs. 1, 3, 5, 1, 4, and 6.

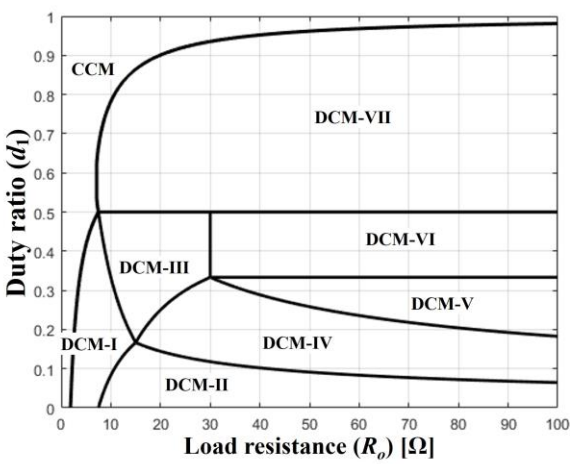

FIGURE 3. Operating regions of two-phase IBC with ICL according to R_o versus d_1 when k = 0.5, L = 100 μH, v_{in} = 100 V and f_s = 25 kHz.

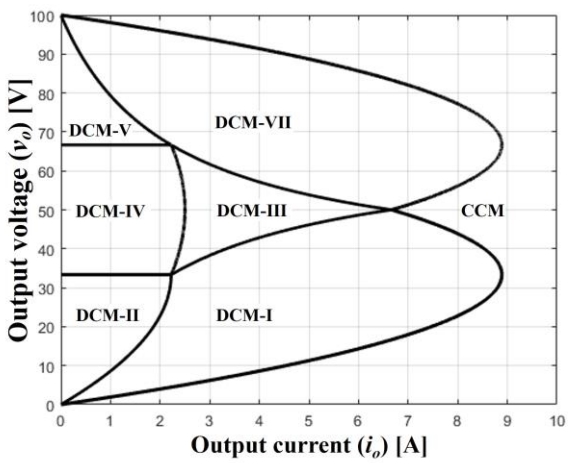

FIGURE 4. Operating regions of two-phase IBC with ICL according to i_o versus v_o when k = 0.5, L = 100 μH, v_{in} = 100 V, and f_s = 25 kHz

III. MATHEMATICAL ANALYSIS

Under the assumption that all active and passive components are ideal, mathematical analysis of IBC with ICL is conducted to obtain the state space averaged models and time interval calculations, and it is verified through simulation.

A. STATE SPACE AVERAGED MODEL

To analyze state space averaged model, di_{L1}/dt and di_{L2}/dt are derived using (2) as follows

$$\begin{cases} \dfrac{di_{L1}}{dt} = \dfrac{v_{L1} + k \cdot v_{L2}}{L\left(1-k^2\right)} \\ \dfrac{di_{L2}}{dt} = \dfrac{v_{L2} + k \cdot v_{L1}}{L\left(1-k^2\right)} \end{cases}. \tag{3}$$

An equation for averaging i_{L1} over T_s is formulated as

$$\frac{dI_{L1}}{dt} = \frac{1}{T_s}\sum_{n=1}^{N} \frac{v_{L1,INTn} + k \cdot v_{L2,INTn}}{L\left(1-k^2\right)}\left(t_n - t_{n-1}\right). \tag{4}$$

Where, I_{L1} denotes average of i_{L1}. $v_{L1,INTn}$ and $v_{L2,INTn}$ represent the v_{L1} and v_{L2} values of the n-th interval, respectively, which can be obtained based on Table I, reflecting the circuit configuration for each interval. In addition, t_n is the n-th time instant given in Table II, and N is total number of intervals for each DCM types.

Thereafter, using KCL, the equation of the capacitor current is derived as

$$C_o \frac{dv_{C_o}}{dt} = i_{L1} + i_{L2} - \frac{v_o}{R_o}. \tag{5}$$

By averaging over T_s for v_{Co}, the following expression (6) is derived where V_{Co} denotes average of v_{Co}.

$$\frac{dV_{C_o}}{dt} = \frac{2I_{L1}}{C_o} - \frac{v_o}{R_o C_o} \tag{6}$$

Since i_{L1} and i_{L2} have a 180° phase difference and the same magnitude over T_s, only either I_{L1} or I_{L2} can be considered to derive (6).

The state space averaged model is in the form:

$$\begin{cases} \dot{\boldsymbol{x}}(t) = \boldsymbol{A}_{av}\boldsymbol{x}(t) + \boldsymbol{B}_{av}v_{in} \\ v_o(t) = \boldsymbol{C}_{av}\boldsymbol{x}(t) \end{cases} \tag{7}$$

where state variables are $\boldsymbol{x}(t) = [i_{L1}\ v_{Co}]^{\mathrm{T}}$, and state matrix, input matrix, and output matrix are denoted by $\boldsymbol{A}_{av}$, $\boldsymbol{B}_{av}$, and $\boldsymbol{C}_{av}$, respectively. In table III, the results of summarizing $\boldsymbol{A}_{av}$ and $\boldsymbol{B}_{av}$ are provided using (4) and (6). Since $v_o = v_{Co}$, the output matrix $\boldsymbol{C}_{av} = [0\ 1]$. $\boldsymbol{A}_{av}$ and $\boldsymbol{B}_{av}$ are represented in Table III excluding d_3 by considering the process of expressing d_3 as a function of d_1 or d_2, which will be mentioned in the following sub-section B.

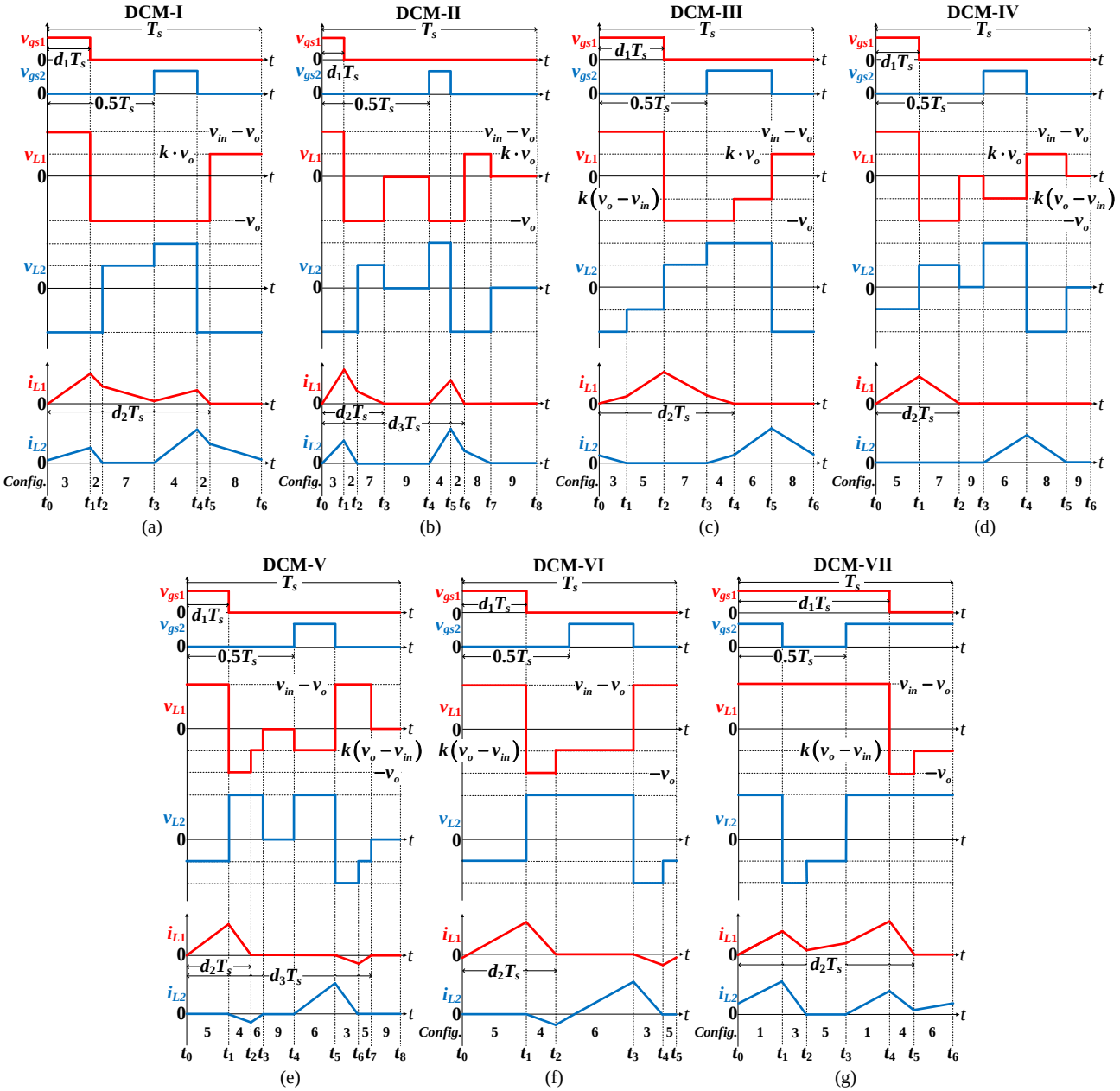

FIGURE 5. Key waveforms in the (a) DCM-Ⅰ, (b) DCM-Ⅱ, (c) DCM-Ⅲ, (d) DCM-Ⅳ, (e) DCM-Ⅴ, (f) DCM-Ⅵ, and (g) DCM-Ⅶ operations.

TABLE II
TIME INSTANTS OF EACH DCM TYPE

DCM type	t_0	t_1	t_2	t_3	t_4	t_5	t_6	t_7	t_8
DCM-I	0	d_1T_s	$(d_2-0.5)T_s$	$0.5T_s$	$(d_1+0.5)T_s$	d_2T_s	T_s	-	-
DCM-II	0	d_1T_s	$(d_3-0.5)T_s$	d_2T_s	$0.5T_s$	$(d_1+0.5)T_s$	d_3T_s	$(d_2+0.5)T_s$	T_s
DCM-III	0	$(d_2-0.5)T_s$	d_1T_s	$0.5T_s$	d_2T_s	$(d_1+0.5)T_s$	T_s	-	-
DCM-IV	0	d_1T_s	d_2T_s	$0.5T_s$	$(d_1+0.5)T_s$	$(d_2+0.5)T_s$	T_s	-	-
DCM-V	0	d_1T_s	d_2T_s	$(d_3-0.5)T_s$	$0.5T_s$	$(d_1+0.5)T_s$	$(d_2+0.5)T_s$	d_3T_s	T_s
DCM-VI	0	d_1T_s	d_2T_s	$(d_1+0.5)T_s$	$(d_2+0.5)T_s$	T_s	-	-	-
DCM-VII	0	$(d_1-0.5)T_s$	$(d_2-0.5)T_s$	$0.5T_s$	d_1T_s	d_2T_s	T_s	-	-

TABLE III
EXPRESSIONS OF STATE SPACE AVERAGED EQUATIONS BY DCM TYPES

DCM type	Expressions of $\boldsymbol{A}_{av}$	Expressions of $\boldsymbol{B}_{av}$
DCM-I	$\begin{bmatrix} 0 & \frac{-(1+k)d_2+k}{L(1-k)} \\ \frac{2}{C_o} & -\frac{1}{R_oC_o} \end{bmatrix}$	$\begin{bmatrix} \frac{d_1}{L(1-k)} \\ 0 \end{bmatrix}$
DCM-II	$\begin{bmatrix} 0 & \frac{-d_2}{L(1-k)} \\ \frac{2}{C_o} & -\frac{1}{R_oC_o} \end{bmatrix}$	$\begin{bmatrix} \frac{d_1}{L(1-k)} \\ 0 \end{bmatrix}$
DCM-III	$\begin{bmatrix} 0 & \frac{-(1+k)d_2+k}{L(1-k)} \\ \frac{2}{C_o} & -\frac{1}{R_oC_o} \end{bmatrix}$	$\begin{bmatrix} \frac{2(1-k)d_1+2k\cdot d_2-k}{2L(1-k)} \\ 0 \end{bmatrix}$
DCM-IV	$\begin{bmatrix} 0 & \frac{-d_2}{L(1-k)} \\ \frac{2}{C_o} & -\frac{1}{R_oC_o} \end{bmatrix}$	$\begin{bmatrix} \frac{d_1}{L} \\ 0 \end{bmatrix}$
DCM-V	$\begin{bmatrix} 0 & \frac{(1+k)(k\cdot d_1-d_2)}{L(1-k)} \\ \frac{2}{C_o} & -\frac{1}{R_oC_o} \end{bmatrix}$	$\begin{bmatrix} \frac{(1-k-k^2)d_1+k\cdot d_2}{L(1-k)} \\ 0 \end{bmatrix}$
DCM-VI	$\begin{bmatrix} 0 & \frac{(1+k)(d_1-d_2)-\frac{1}{2}(1-k)}{L(1-k)} \\ \frac{2}{C_o} & -\frac{1}{R_oC_o} \end{bmatrix}$	$\begin{bmatrix} \frac{1-k-2k(d_1-d_2)}{2L(1-k)} \\ 0 \end{bmatrix}$
DCM-VII	$\begin{bmatrix} 0 & \frac{-(1+k)d_2+k}{L(1-k)} \\ \frac{2}{C_o} & -\frac{1}{R_oC_o} \end{bmatrix}$	$\begin{bmatrix} \frac{d_1+k\cdot d_2-k}{L(1-k)} \\ 0 \end{bmatrix}$

B. CALCULATION OF TIME INTERVAL

Through the state space averaged equations, the voltage second balance (VSB) of L_1 and the charge balance of C_o can be obtained. The process for deriving I_{L1} in the charge balance equation is as follows.

$$I_{L1}=\frac{1}{T_s}\sum_{n=1}^{N}\frac{i_{L1}(t_{n-1})+i_{L1}(t_n)}{2}(t_n-t_{n-1}) \tag{8}$$

To derive (8), the variation in i_{L1} for the n-th interval obtained by integrating (3) over the interval $t_n - t_{n-1}$ can be used. It is expressed as

$$i_{L1}(t_n)-i_{L1}(t_{n-1})=\int_{t_{n-1}}^{t_n}di_{L1}=\int_{t_{n-1}}^{t_n}\frac{v_{L1,INTn}+k\cdot v_{L2,INTn}}{L(1-k^2)}dt. \tag{9}$$

In all DCM types except for DCM-VI, $i_{L1}(0) = i_{L1}(d_2T_s) = i_{L1}(d_3T_s) = i_{L1}(T_s) = 0$. In addition, $i_{L1}(T_s/2) = 0$ for DCM-II, IV, V, and VI, and $i_{L1}((d_1 + 1/2)T_s) = 0$ for DCM-III, IV, V, and VI. Therefore, (8) can be derived using (9). The simplified results of I_{L1} are presented in Table IV. As a result, the two unknowns, d_1 and d_2, and their two simultaneous equations, which are the VSB equation and the charge balance equation substituting I_{L1} equations of Table IV, remain.

In the case of DCM-II and V, the additional equation having unknown d_1, d_2, and d_3 is necessary to eliminate d_3. It can be used that the variation in i_{L1} over T_s is zero because $i_{L1}(T_s) = 0$ in steady state. Since $i_{L1}(d_2T_s) = i_{L1}(d_3T_s) = 0$, a sum of the current variations of the intervals up to d_2T_s is zero, and then the current variations of remaining intervals up to d_3T_s can be added to make an equation which is also zero. In other words, the equations of d_3 can be derived through $i_{L1}(t_5) - i_{L1}(t_4) + i_{L1}(t_6) - i_{L1}(t_5) = 0$ in the case of DCM-II, and $i_{L1}(t_6) - i_{L1}(t_5) + i_{L1}(t_7) - i_{L1}(t_6) = 0$ for DCM-V. These equations can be derived from (9). By substituting these equations into the VSB equation, d_3 can be expressed in terms of d_1 or d_2. Specifically, d_3 is expressed as (10) for DCM-II, and as (11) for DCM-V as follows

$$d_3=\frac{1}{2}+\frac{k\cdot d_2}{(1+k)} \tag{10}$$

$$d_3=\frac{1}{2}+(1+k)d_1. \tag{11}$$

As a result, the only two unknowns, d_1 and d_2, and their two simultaneous equations remain. Therefore, the time interval can be calculated when v_{in}, v_o, L, k, T_s, and R_o are given. The calculation of d_1 and d_2 for all DCM types are summarized in Table V. However, they cannot be determined in the DCM-VI because the output current is not affected by d_1 [20]. By using the equations listed in Table V, the voltage gain of each DCM type can be easily derived based on the VSB of inductor.

C. VERIFICAION OF MATHEMATICAL MODEL BY SIMULATION

By substituting the expressions of d_1, d_2, and d_3 given in Table V, (10), and (11) into the state space averaged equations, V_{Co} and I_{L1} can be calculated. These calculated results are then compared with the PSIM simulation results to verify the mathematical analysis. In the steady state, since $\dot{\boldsymbol{x}}(t) = 0$, V_{Co} and I_{L1} are calculated as $\boldsymbol{x}(t) = -\mathbf{A}_{av}^{-1}\cdot\boldsymbol{B}_{av}\cdot v_{in}$. To compare with the experimental results in Section V, the parameters of the components employed in the experiments are used for calculation and simulation, as shown in Table VI. The experimental tests will be conducted in Section V.

Under these conditions, it is assumed that the IBC with ICL operates over a wide output voltage range to verify all types of DCM. The v_o and d_1 values are set so that DCM types with similar v_o and d_1 ranges have the same v_o and d_1 value. Therefore, v_o is set to 16.8 V for DCM-I and II; 26.4 V for DCM-III and IV; and 31.2 V for DCM-V, VI, and VII, and d_1 is set to 0.15 for DCM-II, IV, and V; 0.3 for DCM-I, III, and VI; and 0.6 for DCM-VII for the calculations and simulations, as listed in Table VII. By substituting the above conditions into

TABLE IV
EXPRESSIONS OF I_{L1} FOR DIFFERENT DCM TYPES

DCM type	Expressions of I_{L1}
DCM-I	$\frac{(1+k)(d_2-d_1)-k}{2L(1-k^2)}d_1 v_{in} T_s$
DCM-II	$\frac{\{k\cdot v_{in}-(1+k)v_o\}d_1+(1-k)d_2 v_o}{2L(1-k^2)}d_2 T_s$
DCM-III	$\frac{-(1-k^2)(v_{in}-v_o)(d_2-1)\left(d_1-d_2+\frac{1}{2}\right)+\{k\cdot v_{in}-(1+k)v_o\}\left(d_2-\frac{1}{2}\right)(d_1-d_2)+\{v_{in}-(1+k)v_o\}\left(d_2-\frac{1}{2}\right)(d_1-d_2+1)}{2L(1-k^2)}T_s$
DCM-IV	$\frac{(v_{in}-v_o)}{2L}d_1 d_2 T_s$
DCM-V	$\frac{(v_{in}-v_o)(1+k)(d_2-k\cdot d_1)}{2L}d_1 T_s$
DCM-VI	$\frac{(d_2-d_1)v_{in}T_s}{4L(1+k)}$
DCM-VII	$\frac{\{(1-k^2)(v_{in}-v_o)(1-d_2)-\sigma_1\}\left(d_1-d_2+\frac{1}{2}\right)+\sigma_1(d_1-1)+\{k\cdot v_{in}-(1+k)v_o\}(d_1-d_2)\left(d_2-\frac{1}{2}\right)+(v_{in}-v_o)\left(d_1-\frac{1}{2}\right)\left(d_2-\frac{1}{2}\right)(1+k)}{2L(1-k^2)}T_s$ where $\sigma_1=\{v_{in}-(1+k)v_o\}(d_1-d_2)-(v_{in}-v_o)\left(d_1-\frac{1}{2}\right)(1+k)$

TABLE V
EXPRESSIONS OF d_1 AND d_2 FOR DIFFERENT DCM TYPES

DCM type	Expressions of d_1	Expressions of d_2
DCM-I	$\frac{v_o\sqrt{L(1-k^2)v_{in}R_o\sigma_1}}{v_{in}R_o\sigma_1}$	$\frac{\sqrt{\frac{L(1-k)(1+k)^3 v_{in}\sigma_1}{R_o}}+k(1+k)\sigma_1}{(1+k)^2\sigma_1}$
DCM-II	$\frac{v_o\sqrt{\frac{L(1-k^2)v_{in}\sigma_1}{R_o}}}{v_{in}\sigma_1}$	$\frac{\sqrt{L(1-k^2)v_{in}R_o\sigma_1}}{R_o\sigma_1}$
DCM-III	$\frac{\sqrt{\frac{v_{in}\{(1+k)v_o-k\cdot v_{in}\}\{4\cdot L(1+k)^2 v_o-k\cdot v_{in}R_oT_s\}\sigma_1}{R_o}}}{2(1+k)v_{in}\sigma_1}+\frac{k\cdot v_{in}\sigma_1}{2(1+k)v_{in}\sigma_1}$	$\frac{-(1-k)\sqrt{v_{in}R_o\sigma_1\{k\cdot v_{in}-(1+k)v_o\}(k\cdot v_{in}R_oT_s-4\cdot L\cdot\sigma_2)}}{2(1+k)\sigma_3}+\frac{2\cdot k\cdot\sigma_3}{2(1+k)\sigma_3}$
DCM-IV	$\frac{L\cdot v_o}{\sqrt{L\cdot v_{in}(v_{in}-v_o)R_oT_s}}$	$\frac{\sqrt{L\cdot v_{in}(v_{in}-v_o)R_oT_s}}{(v_{in}-v_o)R_oT_s}$
DCM-V	$\frac{\sqrt{L\cdot v_o\{(1+k)v_o-k\cdot v_{in}\}R_o\sigma_4}}{R_o\sigma_4}$	$\frac{\{(1-k)v_{in}+k\cdot\sigma_5\}\sqrt{\frac{L\cdot v_o\sigma_4\sigma_5}{R_o}}}{\sigma_4\sigma_5}$
DCM-VI	$d_2-\frac{\sqrt{\sigma_6^2+(k\cdot L\cdot\sigma_7)^2+2\cdot L(2+k)\sigma_6\sigma_7}+k\cdot L\cdot\sigma_7-\sigma_6}{R_oT_s\sigma_7}$	$d_1+\frac{\sqrt{\sigma_6^2+(k\cdot L\cdot\sigma_7)^2+2\cdot L(2+k)\sigma_6\sigma_7}+k\cdot L\cdot\sigma_7-\sigma_6}{R_oT_s\sigma_7}$
DCM-VII	$\frac{\sqrt{\frac{L(1+k)^2(1-k)v_{in}v_o\sigma_5\sigma_8}{R_o}}+k\cdot v_{in}\sigma_8}{(1+k)v_{in}\sigma_8}$	$\frac{\sqrt{L(1+k)^2(1-k)v_{in}v_oR_o\sigma_5\sigma_8}+k\cdot R_o\sigma_5\sigma_8}{(1+k)R_o\sigma_5\sigma_8}$

where $\sigma_1=\{v_{in}-(1+k)v_o\}T_s$; $\sigma_2=(1+k)^2 v_o$; $\sigma_3=\{k\cdot v_{in}{}^2-\sigma_2(v_{in}-v_o)\}R_oT_s$; $\sigma_4=v_{in}(1-k^2)(v_{in}-v_o)T_s$; $\sigma_5=(1+k)v_o-k\cdot v_{in}$; $\sigma_6=(1-k)R_oT_s$; $\sigma_7=4(1+k)$; $\sigma_8=(1+k)(v_{in}-v_o)T_s$.

TABLE VI
SPECIFICATIONS OF PARAMETERS USED IN SIMULATION AND EXPERIMENT

Input voltage (v_{in})	48 V
Switching frequency (f_s)	25 kHz
Inductors ($L = L_1 = L_2$)	72.3 μH
Coupling factor (k)	0.744
Output filter capacitor (C_o)	400 μF

TABLE VII
CONDITIONS AND RESULTS OF CALCULATED AND SIMULATED VALUES OF V_{Co} AND I_{L1} IN ALL DCM TYPES

DCM type	Set-up condition of d_1	Set-up condition of v_o	$R_{o,cal}$	$V_{Co,cal}$	$V_{Co,sim}$	$I_{L1,cal}$	$I_{L1,sim}$
DCM-I	0.3	16.8 V	2.8193 Ω	16.8000 V	16.8078 V	2.9795 A	2.9818 A
DCM-II	0.15	16.8 V	11.2772 Ω	16.8000 V	16.8038 V	0.7449 A	0.7465 A
DCM-III	0.3	26.4 V	15.8861 Ω	26.4000 V	26.4030 V	0.8309 A	0.8317 A
DCM-IV	0.15	26.4 V	54.0019 Ω	26.4000 V	26.4006 V	0.2444 A	0.2452 A
DCM-V	0.15	31.2 V	130.1888 Ω	31.2000 V	31.2049 V	0.1198 A	0.1202 A
DCM-VI	0.3	31.2 V	35.6377 Ω	31.2000 V	31.1967 V	0.4377 A	0.4383 A
DCM-VII	0.6	31.2 V	6.3851 Ω	31.2000 V	31.2045 V	2.4432 A	2.4431 A

the d_1 equations of Table V, the R_o values of all DCM types are calculated, which are also shown in Table VII. However, it can be observed from Table IV and V that the output current does not vary with d_1 for DCM-VI. Therefore, v_o of DCM-VI is determined by the simulation specifications of Table VI and R_o regardless of d_1. However, within the duty range where the converter operates in DCM-VI, d_1 is assumed to be 0.3 to maintain a consistent value similar to other DCM types, and calculations and simulations are conducted accordingly. The results of calculations and simulations are also summarized in Table VII.

In Table VII, $R_{o,cal}$ represents the calculated R_o value based on the set-up conditions of d_1 and v_o, while $V_{Co,cal}$ and $I_{L1,cal}$ denote the calculated results. The simulation results are denoted as $V_{Co,sim}$ and $I_{L1,sim}$. Since there is no significant error between the calculation results and the simulation results, the validity of the mathematical analysis is verified.

IV. BOUNDARY CONDITIONS

After d_1 and d_2 are obtained in Section III, the boundary conditions between adjacent DCM types (including the CCM) can be established. There are ten borders, as shown in Fig. 3. Then, the boundary condition for each border is analyzed as follows.

- CCM and DCM-I: Distinguishing the DCM-I from the CCM involves checking whether d_2 is greater than 1. If so, it means that i_{L1} and i_{L2} do not reach zero, and the converter operates as the CCM.
- CCM and DCM-VII: As in the above case, whether d_2 is greater than 1 determines the boundary condition.
- DCM-I and DCM-II: It depends on whether i_{L1} is zero at $0.5T_s$. If so, the IBC operates in the DCM-II. In particular. this boundary condition can be derived by adding the current variations of DCM-I for the intervals up to half period. It is expressed as $v_o/v_{in} > 2 \cdot d_1$.
- DCM-I and DCM-III: It can be distinguished by checking whether i_{L1} becomes zero after Q_2 is turned off. When the IBC operates in the DCM-III, i_{L1} becomes zero whereas Q_2 is ON. This boundary condition is represented as $d_2 < (d_1 + 0.5)$.
- DCM-II and DCM-IV: It depends on whether the values of v_{L1} at the fifth and sixth intervals for DCM-II and at the fourth interval for DCM-IV are different, which are $-v_o$ and $k(v_o - v_{in})$, respectively. For example, if $k(v_o - v_{in})$ is greater than $-v_o$ at the fourth interval of DCM-IV, the converter operates as the DCM-IV. It is expressed as $v_o/v_{in} > k/(1 + k)$.
- DCM-III and DCM-IV: It is determined based on whether d_2 is less than 0.5. If so, the converter operates as the DCM-IV. Then, this boundary condition is described as $v_o/v_{in} > 2 \cdot d_1$.
- DCM-III and DCM-VI: The values of v_{L1} are different at the last interval for DCM-III and last two intervals for DCM-VI. They are $k \cdot v_o$ and $v_{in} - v_o$, respectively. If $k \cdot v_o$ is greater than $v_{in} - v_o$, the converter operates in the DCM-VI. It is represented as $v_o/v_{in} > 1/(1 + k)$.
- DCM-IV and DCM-V: Similarly, the values of v_{L1} are different at the fifth interval of DCM-IV and the sixth and seventh intervals of DCM-V. In order to operate as the DCM-V, $k \cdot v_o$ must be greater than $v_{in} - v_o$ at the fifth interval of DCM-IV. This is expressed as $v_o/v_{in} > 1/(1 + k)$.
- DCM-V and DCM-VI: This boundary condition depends on whether d_3T_s is within T_s. In other words, if $d_3 > 1$, the converter operates in the DCM-VI. It is represented as $d_1 > 1/[2(1 + k)]$.
- DCM-VII and DCM-III or DCM-VI: To distinguish the DCM-VII from DCM-III or DCM-VI, it depends on whether d_1 is greater than 0.5. That is, if $d_1 > 0.5$, the IBC operates in the DCM-VII.

By considering all boundary conditions described in above, the operating regions of IBC with the relationship between d_1 and the input-output voltage conversion ratio (v_o/v_{in}) are shown in Fig. 6 according to three different values of k. By calculating VSB using the state space averaged equations in

Table III, it can be seen that v_o/v_{in} is determined solely by k, d_1, and d_2. Since d_1 is represented as a value between 0 and 1, and d_2 is substituted into VSB as a value of 1, 0.5, and d_1 + 0.5 for the boundary conditions, the boundary conditions can only change due to k, as shown in Fig. 6.

In addition, by utilizing the boundary conditions between CCM and DCM-I, and between CCM and DCM-VII, the self-inductance value can be derived when $d_2 = 1$ to calculate the maximum self-inductance value ($max\{L\}$) required for DCM operation. $max\{L\}$ can be formulated using the equations in Table V as

$$max\{L\} = \begin{cases} \dfrac{v_{in} - (1+k)v_o}{v_{in}(1-k^2)} R_o T_s, & \text{for } d_1 < 0.5 \\ \dfrac{(v_{in} - v_o)\{v_o - k(v_{in} - v_o)\}}{v_{in} v_o (1-k^2)} R_o T_s, & \text{for } d_1 \geq 0.5 \end{cases} . \quad (12)$$

V. EXPERIMENTAL RESULTS

As shown in Fig. 7, the hardware prototype of two-phase IBC with ICL is implemented to carefully examine whether all DCM types change at boundary conditions, and whether they appear while operating in the DCM. Its parameters are listed in Table VI. Two switches, Q_1 and Q_2, are implemented by using the metal oxide semiconductor field effect transistors (MOSFETs) with the optocoupler ICs of FOD3180. The part numbers of MOSFETs, and diodes are FDPF680N10T and SDT10100CT, respectively. The coupled inductor is made by two U-cores, and it has the coupling factor, k of 0.744 and self-inductance of $L = L_1 = L_2 = 72.3$ μH. The experimental tests are designed to be conducted below 250 W. The point of maximum power among expected measurement points for the experimental tests is on the boundary between CCM and DCM-VII when v_o = 31.2 V and d_1 = 0.65. At the point, $max\{L\}$ is calculated as 73.2 μH. Therefore, the coupled inductor is made to have self-inductance values as close as possible to calculated $max\{L\}$. Also, the value of C_o is 400 μF having $\pm$10 % tolerance. The electric load is used to adjust R_o for load condition variation. Then, the digital signal processor (DSP) of TMS320F28377S is used to generate the pulse-width-modulation (PWM) control signals.

To validate the boundary conditions, the value of d_1 (by which the DCM type changes) is measured by increasing R_o, and experimental results are needed to show the boundary condition between DCM-I and II with $v_o/v_{in} < k/(1 + k)$. In addition, results with $k/(1 + k) < v_o/v_{in} < 0.5$ are required to demonstrate the boundary conditions for DCM-I, III, and IV. To measure the boundary conditions for DCM-VII, III, and IV, experimental results with $0.5 < v_o/v_{in} < 1/(1 + k)$ are needed, and finally, to measure the boundary conditions for DCM-VII, VI, and V, results with $v_o/v_{in} > 1/(1 + k)$ are required. To ensure equal intervals for the four cases with the coupled inductor used in the experiment, experiments are conducted with voltage ratios of 0.35, 0.45, 0.55, and 0.65. Note that they are

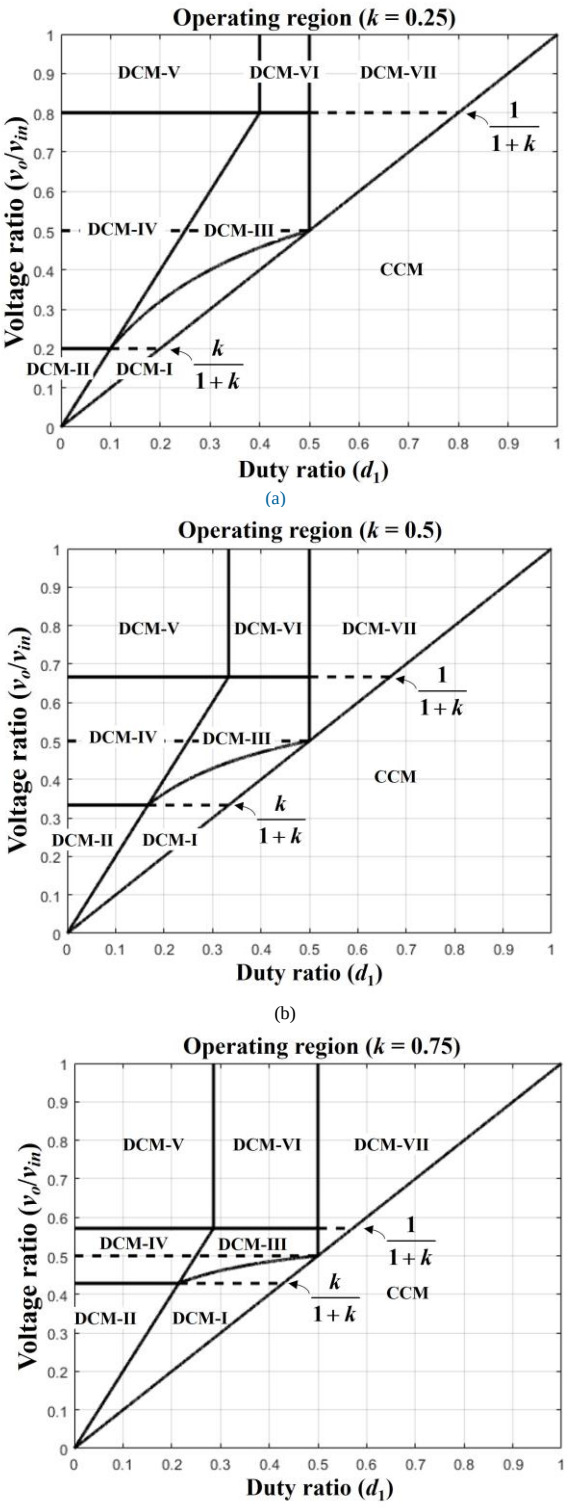

FIGURE 6. Operating regions of IBC with ICL based on d_1 versus v_o/v_{in} for (a) k = 0.25, (b) 0.5, and (c) 0.75.

maintained by controlling v_o based on the closed-loop proportional-integral (PI) controller of DSP. The experimental results are shown in Fig. 8, and they are compared with the theoretical values.

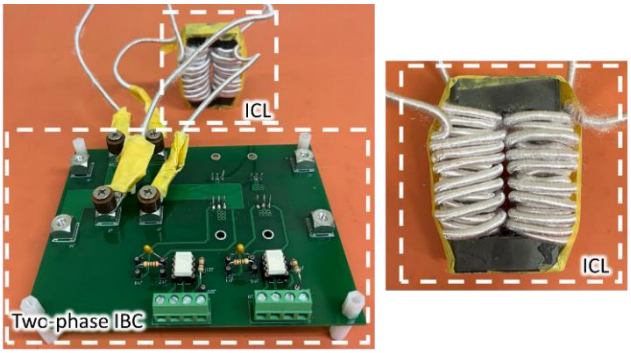

FIGURE 7. Experimental prototype of the two-phase IBC with ICL.

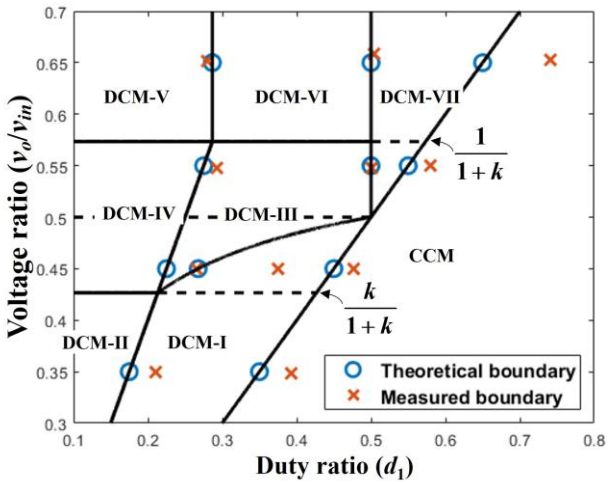

FIGURE 8. Experimental results to find the value of d_1 by which DCM type changes and comparison with theoretical values.

It is clearly observed from the result of Fig. 8 that the experimental results have good agreement with the theoretical values at boundary conditions. In particular, their values between the DCM-V and DCM-VI matches well. Nevertheless, they are still slightly different at some boundary conditions. This is because there exist various non-idealities of MOSFETs, diodes, and resistances of passive elements. In addition, the ringing of inductor voltages (which are shown in the below experimental results) might cause to make this error.

The measured waveforms (v_{gs1}, i_{in}, v_{L1}, v_{L2}, i_{L1}, i_{L2}, and v_o) for all DCM types are shown from Figs. 9 to 15, where the black-dotted line represents the theoretically expected waveform of v_{L1}. The measured values of d_1, d_2, and d_3 are obtained through the measured waveforms of v_{gs1} and i_{L1}. I_{in} is measured for efficiency calculation. The efficiency for each DCM types is calculated as $v_o \cdot i_o / v_{in} \cdot i_{in}$, assuming v_{in} = 48 V and $i_o = 2 \cdot i_{L1}$. The v_{L1} and v_{L2} waveforms are measured to verify DCM types. The measured v_o values is used for the calculations of theoretical values. Note that the experimental tests are conducted by changing the values of R_o, while keeping v_o/v_{in} constant. To compare the measured values with the calculated and simulated values, the experiments are conducted using the calculated R_o and v_o values from Table VII. As mentioned above, DCM-VI can appear when the IBC is operated by open-loop controller. Therefore, the waveforms of DCM-VI are measured when the converter is operating under open-loop control. They are compared with the theoretical values of d_1, d_2, and d_3 ($d_{1,cal}$, $d_{2,cal}$, and $d_{3,cal}$), which are calculated by mathematical expressions in Table V. Due to the resolution limitations of the electric load, R_o values are set-up to the second decimal place. Then, they are calculated by the R_o values and measured v_o values and summarized in Table VIII. In particular, for the DCM-VI, $d_{1,cal}$ cannot be calculated, as mentioned previously. Thus, $d_{2,cal}$ is calculated by assuming that $d_{1,cal} = d_1 = 0.3008$.

Although there is a slight discrepancy between the calculated and measured values, the black-dotted line, which is theoretical waveform of v_{L1}, and waveforms of i_{L1} and i_{L2} verify that all seven DCM types can be observed depending on v_o/v_{in} and the load conditions.

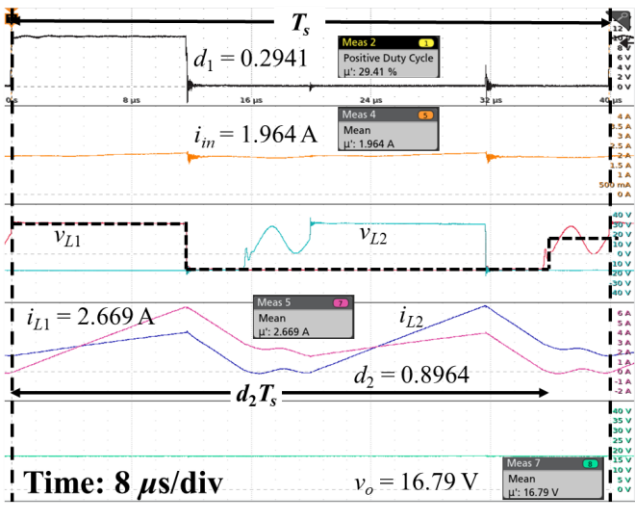

FIGURE 9. Experimental results of DCM-Ⅰ while v_o/v_{in} = 0.35 and R_o = 2.82 Ω.

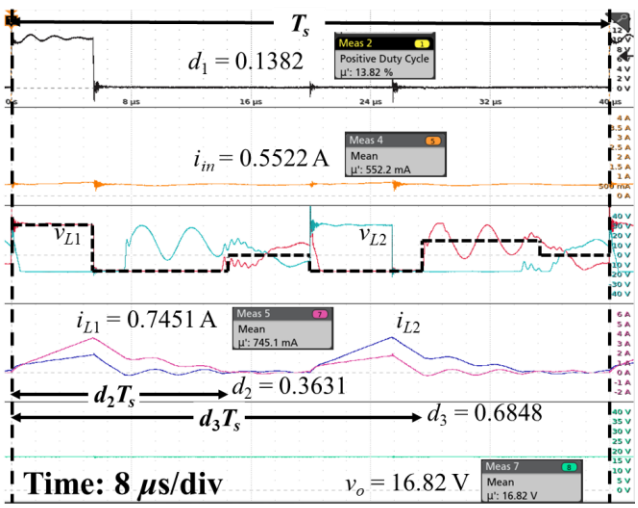

FIGURE 10. Experimental results of DCM-Ⅱ while v_o/v_{in} = 0.35 and R_o = 11.28 Ω.

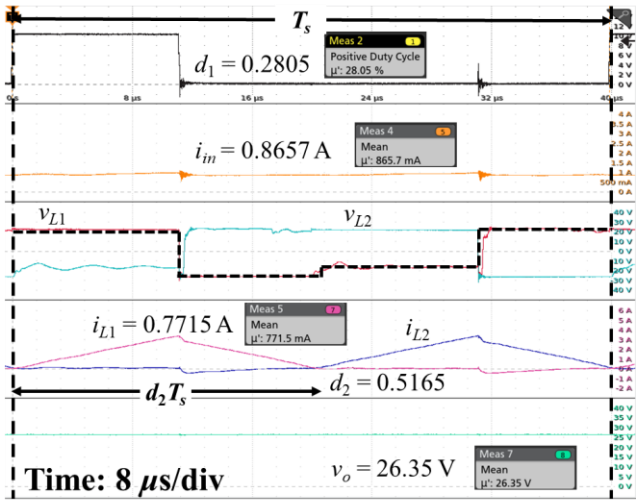

FIGURE 11. Experimental result of DCM-Ⅲ while v_o/v_{in} = 0.55 and R_o = 15.89 Ω.

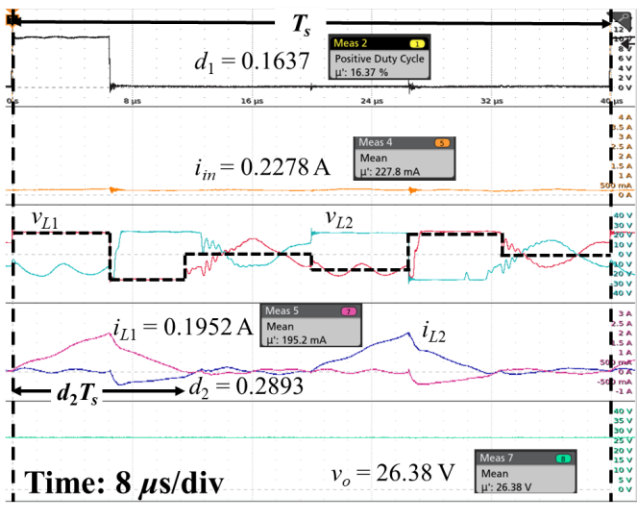

FIGURE 12. Experimental results of DCM-Ⅳ while v_o/v_{in} = 0.55 and R_o = 54 Ω.

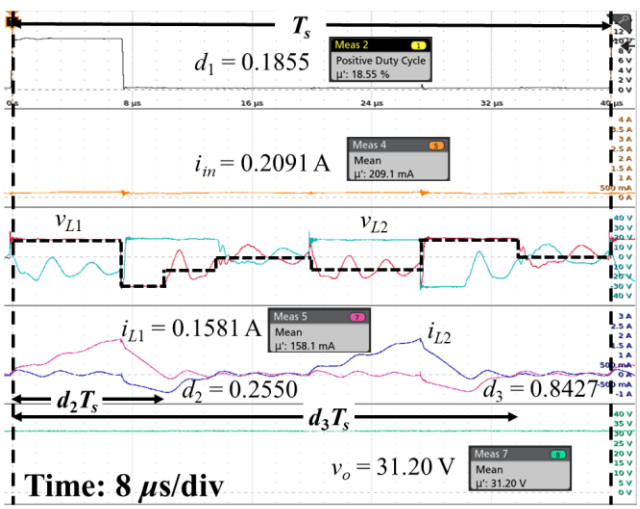

FIGURE 13. Experimental results of DCM-Ⅴ while v_o/v_{in} = 0.65 and R_o = 130.19 Ω.

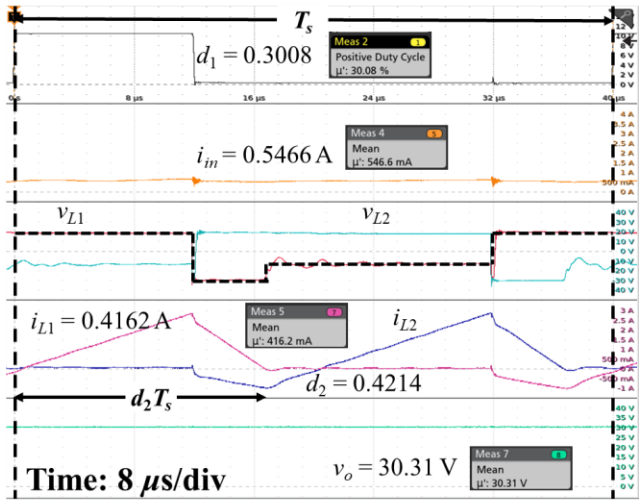

FIGURE 14. Experimental results of DCM-Ⅵ while v_o/v_{in} = 0.65 and R_o = 35.64 Ω.

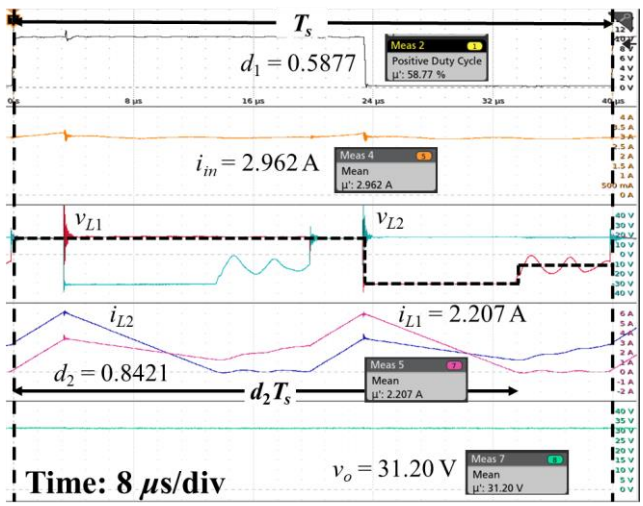

FIGURE 15. Experimental results of DCM-Ⅶ while v_o/v_{in} = 0.65 and R_o = 6.39 Ω.

VI. CONCLUSION

This study made the detailed analysis of two-phase interleaved buck converter (IBC) with an inversely coupled inductor (ICL) operating in the discontinuous conduction modes (DCMs). Also, the associated circuit configurations with different DCM operations were described. Then, all possible DCM types, which can vary with the combinations of circuit configurations, were analyzed. In particular, a mathematical analysis was conducted using state space averaged modeling and time interval calculations, and it was verified through simulation. In addition, the boundary conditions between adjacent DCM types or even CCM were analyzed, enabling the design of the maximum self-inductance required for DCM operation. The analysis method proposed in this paper, which distinguishes the DCM types of the converter based on the combinations of circuit configurations, is expected to be extended to other topologies using coupled inductor.

TABLE VIII
COMPARISON OF MEASUREMENTS AND CALCULATED VALUES OF d_1, d_2, AND d_3 IN ALL DCM TYPES

DCM type	R_o	v_o	d_1	$d_{1,cal}$	d_2	$d_{2,cal}$	d_3	$d_{3,cal}$	Efficiency
DCM-I	2.82 Ω	16.79 V	0.3000	0.2941	0.9178	0.8964	-	-	95.07 %
DCM-II	11.28 Ω	16.82 V	0.1503	0.1382	0.4289	0.3631	0.6830	0.6848	94.57 %
DCM-III	15.89 Ω	26.35 V	0.2937	0.2805	0.5231	0.5165	-	-	97.84 %
DCM-IV	54.00 Ω	26.38 V	0.1498	0.1637	0.2726	0.2893	-	-	94.19 %
DCM-V	130.19 Ω	31.20 V	0.1500	0.1855	0.2102	0.2550	0.7616	0.8427	98.29 %
DCM-VI	35.64 Ω	30.31 V	0.3008	0.3008	0.4158	0.4214	-	-	96.16 %
DCM-VII	6.39 Ω	31.20 V	0.5999	0.5877	0.8715	0.8421	-	-	96.86 %

The comprehensive DCM study for the two-phase IBC with ICL was fully verified by experimental test under various load conditions and different input/output voltage conversion ratios. In particular, it would be expected that the proposed mathematical analysis and boundary condition can be preferably used for designing the proper closed-loop controller for the two-phase IBC with ICL in practice. In addition, as presented in [10], IBC with ICL is expected to have higher efficiency than IBC only in limited regions, similar to the CCM operation. Therefore, further study on efficiency analysis and detailed converter design is needed to optimize the operating regions of IBC with ICL. As a result, the operation and control performance of converter in the DCMs can be further enhanced.

REFERENCES

[1] O. Hegazy, J. V. Mierlo and P. Lataire, "Analysis, Modeling, and Implementation of a Multidevice Interleaved DC/DC Converter for Fuel Cell Hybrid Electric Vehicles," *IEEE Trans. Power Electron.*, vol. 27, no. 11, pp. 4445–4458, Nov. 2012.

[2] P. W. Lee, Y. S. Lee, D. K. W. Cheng and X. C. Liu, "Steady-state analysis of an interleaved boost converter with coupled inductors," *IEEE Trans. Ind. Electron.*, vol. 47, no. 4, pp. 787–795, Aug. 2000.

[3] X. Yang, S. Zong and G. Fan, "Analysis and validation of the output current ripple in interleaved buck converter," *IECON 2017 - 43rd Annual Conf. IEEE Ind. Electron. Society*, Beijing, China, 2017, pp. 846-851.

[4] M. Beres, D. Kovac, T. Vince, I. Kovacova, J. Molnar, I. Tomchikova, J. Dziak, P. Jacko, B. Fecko, and S. Gans, "Efficiency enhancement of non-isolated DC-DC interleaved buck converters for renewable energy sources," *Energies*, vol. 14, pp. 4127–4141. Jul. 2021.

[5] M. N. Syah, E. Firmansyah, and D. R. Utomo, "Interleaved bidirectional DC-DC converter operation strategies and problem challenges: an overview," *2022 IEEE International Conference in Power Engineering Application (ICPEA)*, Shah Alam, Malaysia, 2022, pp. 1–6.

[6] M. Biswas, S. Majhi and H. B. Nemade, "Performance of a coupled inductor for interleaved buck converter with improved step-down conversion ratio," *IET Power Electron.*, vol. 14, pp. 239–256, Feb. 2021.

[7] M. Biswas, S. Majhi and H. B. Nemade, "A high step-down DC–DC converter with reduced inductor current ripple and low voltage stress," *IEEE Trans. Ind. Appl.*, vol. 57, no. 2, pp. 1559–1571, March-April 2021.

[8] Z. Dai, J. Liu, K. Li, Z. Mai and G. Xue, "Research on a modeling and control strategy for interleaved boost converters with coupled inductors," *Energies*, vol. 16, pp. 3810–3825. Apr. 2023.

[9] T. Kang and Y. Suh, "Optimized coupling factor design of multiple-phase coupled inductor for minimum inductor current ripple operation in EV charger systems," *2017 IEEE 3rd International Future Energy Electron. Conf. ECCE Asia (IFEEC 2017-ECCE Asia)*, Kaohsiung, Taiwan, 2017, pp. 1178–1183.

[10] P. L. Wong, P. Xu, P. Yang, and F. C. Lee, "Performance improvements of interleaving VRMs with coupling inductors," *IEEE Trans. Power Electron.*, vol. 16, no. 4, pp. 499–507, Jul. 2001.

[11] H. Seok, S. Kim, W. S. Choi, M. J. Kim, J. S. Lee and M. Kim, "Coupled inductor based multi-phase buck converter for magnet power supply," *2017 IEEE Applied Power Electron. Conf. Expo. (APEC)*, Tampa, FL, USA, 2017, pp. 1020–1026.

[12] J. W. Kolar, G. R. Kamath, N. Mohan, and F. C. Zach, "Self-adjusting input current ripple cancellation of coupled parallel connected hysteresis-controlled boost power factor correctors," in *Proc. Power Electron. Spec. Conf. (PESC)*, Atlanta, GA, USA, 1995, pp. 164–173.

[13] E. Laboure, A. Cuniere, T. A. Meynard, F. Forest, and E. Sarraute, "A theoretical approach to intercell transformers, application to interleaved converters," *IEEE Trans. Power Electron.*, vol. 23, no. 1, pp. 464–473, Jan. 2008.

[14] H. Kosai, S. Mcneal, B. Jordan, J. Scofield, B. Ray, and Z. Turgut, "Coupled inductor characterization for a high performance interleaved boost converter," *IEEE Trans. Magn.*, vol. 45, no. 10, pp. 4812–4815, Oct. 2009.

[15] D. O. Boillat and J. W. Kolar, "Modeling and experimental analysis of a coupling inductor employed in a high performance AC power source," *2012 Int. Conf. Renewable Energy Res. Appl. (ICRERA)*, Nagasaki, Japan, 2012, pp. 1–18.

[16] M. Chorishiya and D. K. Palwalia, "Analysis of interleaved coupled inductor ultra-boost converter for solar PV applications," *2019 2nd Int. Conf. Power Energy, Environ. Int. Ctrl. (PEEIC)*, Greater Noida, India, 2019, pp. 351–355.

[17] R. Mayer, M. B. E. Kattel and S. V. G. Oliveira, "Multiphase interleaved bidirectional DC/DC converter with coupled inductor for electrified-vehicle applications," *IEEE Trans. Power Electron.*, vol. 36, no. 3, pp. 2533–2547, Mar. 2021.

[18] F. Yang, X. Ruan, G. Wu and Z. Ye, "Discontinuous-current mode operation of a two-phase interleaved boost DC–DC converter with coupled inductor," *IEEE Trans. Power Electron.*, vol. 33, no. 1, pp. 188–198, Jan. 2018.

[19] X. Huang, X. Wang, T. Nergaard, J. S. Lai, X. Xu and L. Zhu, "Parasitic ringing and design issues of digitally controlled high power interleaved boost converters," *IEEE Trans. Power Electron.*, vol. 19, no. 5, pp. 1341–1352, Sep. 2004.

[20] B. C. Barry, J. G. Hayes and M. S. Ryłko, "CCM and DCM operation of the interleaved two-phase boost converter with discrete and coupled inductors," *IEEE Trans. Power Electron.*, vol. 30, no. 12, pp. 6551–6567, Dec. 2015.

[21] B. Ray, H. Kosai, S. McNeal, B. Jordan and J. Scofield, "A comprehensive multi-mode performance analysis of interleaved boost converters," *2010 IEEE Energy Conversion Cong. Expo.(ECCE)*, Atlanta, GA, USA, 2010, pp. 3014–3021.

[22] D. Wu, G. Calderon-Lopez, and A. J. Forsyth, "Discontinuous conduction/current mode analysis of dual interleaved buck and boost converters with interphase transformer," *IET Power Electron.*, vol. 9, no. 1, pp. 31–41, Jan. 2015.

[23] B. C. Barry et al., "Small-signal model of the two-phase interleaved coupled-inductor boost converter," *IEEE Trans. Power Electron.*, vol. 33, no. 9, pp. 8052–8064, Sep. 2018.

[24] P. Azer and A. Emadi, "Generalized state space average model for multi-phase interleaved buck, boost and buck-boost DC-DC converters: transient, steady-state and switching dynamics," *IEEE Access*, vol. 8, pp.77735–77745, 2020.

[25] H. Dan, S. Zhou, J. Xu, S. We, Y. Sun, and M. Su, "Stability Analysis of the interleaved buck converter with coupled inductor," *IEEE Trans. Emerg. Sel. Topics Power Electron.*, vol. 9, no. 4, pp. 4658–4667, Aug. 2021.

HYE-CHEON KIM (Student Member, IEEE) received the B. S. degree from the School of Electrical Engineering, Soongsil University, Seoul, South Korea, in 2014. He is currently working toward the Ph.D. degree in the Department of Electrical and Electronic Engineering, Yonsei University, Seoul, South Korea, via the combined M.S. and Ph.D. program. His research interests include DC-DC converters, electric vehicle power conversion system and control of grid-connected converters.

MRIGANKA BISWAS (Member, IEEE) received the B.Tech. degree in electrical engineering from the West Bengal University of Technology, West Bengal, India, in 2012, and the M.E. degree in electrical engineering (control systems) from the Birla Institute of Technology Mesra, Ranchi, India, in 2014. He obtained a PhD degree in power electronics and control systems from the Department of Electronics and Electrical Engineering, Indian Institute of Technology Guwahati, Guwahati, India in 2021.

He was a Post-graduate (M.E.) Project Fellow with Variable Energy Cyclotron Centre, DAE, Kolkata, India, during 2013–2014. Dr. Biswas has been awarded GATE and Visvesvaraya Fellowship for his master's and doctoral program respectively by MHRD and MEITY, Govt. Of India. He was a postdoctoral research associate in the Department of Electrical and Electronics Engineering at Yonsei University, South Korea. Dr. Biswas has been awarded a BK21 fellowship by the Korean Research Foundation, Govt. of the Republic of Korea (South). At present, Dr. Biswas is a research associate at the Institute for Energy Systems, The University of Edinburgh, United Kingdom. His research interests include DC-DC converter topology, diode/switched-capacitor cells, coupled inductors, control of DC-DC power converters, AC-DC converter design and control, EV/HEV and offshore wind turbine applications.

JUNG-WOOK PARK (Senior Member, IEEE) was born in Seoul, South Korea. He received the B.S. degree (*summa cum laude*) from the Department of Electrical Engineering, Yonsei University, Seoul, in 1999, and the M.S.E.C.E. and Ph.D. degrees from the School of Electrical and Computer Engineering, Georgia Institute of Technology, Atlanta, GA, USA, in 2000 and 2003, respectively. From 2003 to 2004, he was a Postdoctoral Research Associate with the Department of Electrical and Computer Engineering, University of Wisconsin–Madison, Madison, WI, USA. Since 2005, he has been with the School of Electrical and Electronic Engineering, Yonsei University, where he is currently a professor. His current research interests include power system dynamics, energy management systems, renewable energies-based distributed generation systems, and hardware implementation of power-electronic based inverters, etc.

Prof. Park was the recipient of the Young Scientist Presidential Award in 2013 from the Korean Academy of Science and Technology (KAST), South Korea. He is also the Director at the Yonsei Power System Research Center of Great Energy Transition (Yonsei-PREFER) supported by the leading research program (with the $7.2M USD grant for 9 years from 2020 to 2029) of the National Research Foundation (NRL), South Korea.